International Journal of Minerals, Metallurgy and Materials
Volume 24, Number 10, October 2017, Page 1145
DOI: 10.1007/s12613-017-1505-3

Tempering stability of Fe–Cr–Mo–W–V hot forging die steels

Yuan-ji Shi, Xiao-chun Wu, Jun-wan Li, and Na Min

School of Materials Science and Engineering, Shanghai University, Shanghai 200072, China
(Received: 21 January 2017; revised: 25 April 2017; accepted: 27 April 2017)

Abstract: The tempering stability of three Fe–Cr–Mo–W–V hot forging die steels (DM, H21, and H13) was investigated through hardness measurements and transmission electron microscopy (TEM) observations. Both dilatometer tests and TEM observations revealed that DM steel has a higher tempering stability than H21 and H13 steels because of its substantial amount of M_2C (M represents metallic element) carbide precipitations. The activation energies of the M_2C carbide precipitation processes in DM, H21, and H13 steels are 236.4, 212.0, and 228.9 kJ/mol, respectively. Furthermore, the results indicated that vanadium atoms both increase the activation energy and affect the evolution of M_2C carbides, resulting in gradual dissolution rather than over-aging during tempering.

Keywords: tempering stability; hot forging; die steels; carbide precipitation

1. Introduction

As basic equipment in the mechanical industry, hot forging dies are mainly used for solid metal shaping at temperatures above the recrystallization temperature of the material; such shaping is extensively used in the automotive and machinery manufacturing industries. Hot forging dies are inevitably subjected to mechanical loadings at high temperatures under service; the local temperature of the die surface can exceed 600°C [1]. Tempering stability is widely studied as an important indicator of the high-temperature performance of hot forging die materials. Nanosized secondary carbides dispersed within the microstructure can substantially improve the tempering stability [2]. Therefore, Fe–Cr–Mo–W–V hot forging die steels were selected as die steels on the basis of their high tempering stability, and our knowledge of their tempering stability relies on our understanding of their diffusional phase transformation during tempering.

Early studies related to phase transformations in steels during tempering were mainly focused on the four principal transformations of Fe–C martensite [3–6]: (1) segregation of carbon atoms in martensite; (2) decomposition of martensite and formation of metastable ε-carbide ($Fe_{2.4}C$); (3) transformation of residual austenite; (4) and formation of cementite (Fe_3C). In recent decades, researchers have shown increased interest in attaining a more fundamental understanding of the various precipitate particles' transformations in steels with different compositions when the steels are subjected to different heat-treatment and service conditions. For instance, Ghost *et al.* [7] utilized the Thermo-Calc software to calculate the nucleation driving forces of quasi-equilibrium cementite and found that Si decreases the driving force of cementite nucleation, whereas C, Mn, and Cr markedly increase the driving force. Björklund *et al.* [8] derived a theoretical expression on the coarsening kinetics of cementite in the α matrix of Fe–M–C ternary systems by assuming an equilibrium partitioning of alloy elements between cementite and ferrite. They found that the volume diffusion of alloy elements in the α matrix for the partitioning serves as the controlling process for the coarsening of cementite. This result is consistent with those of other researchers [9–11] who concluded that the growth of cementite is remarkably retarded by the addition of Mn, Cr, and Si. In addition, Pilling *et al.* [12] reported that the microstructural and compositional features during tempering at 700°C are not fully consistent with the precipitation sequence reported by Baker and Nutting [13] for commercial 2.25Cr–1Mo steels. Inoue *et al.* [14] used transmission electron microscopy (TEM) to clarify the transformation process

Corresponding author: Yuan-ji Shi E-mail: syuanj@163.com

of the Cr-based carbides $M_3C \rightarrow M_7C_3 \rightarrow M_{23}C_6 \rightarrow M_6C$ and their crystallographic relationships. In particular, the $M_{23}C_6$ and M_7C_3 structural components, which are recognized as the main precipitate phases in high-carbon Cr-based steels, were intensively analyzed. Grain boundaries can be strengthened by block-shaped $M_{23}C_6$ at high temperatures [15–17]. By contrast, M_7C_3 carbide is enriched with Cr and grows more quickly than other carbide alloys [18–20]. In addition, Mukherjee [21] showed that the addition of Mo results in an increased tendency to form $M_{23}C_6$ at the expense of M_7C_3 in high-Cr steels. A similar phenomenon was recently observed by Zhang *et al.* [22], who claimed that the optimum conditions for precipitation of the metastable $M_{23}C_6$ phase are a lower Cr content and a higher Mo content in a ferritic matrix. Furthermore, many researchers have studied the effect of V on carbides. Zhang *et al.* [23] proposed that the precipitation of M_6C carbides containing V suppresses the precipitation of M_7C_3 carbides. Ishii *et al.* [24] reported that the type of fine precipitates formed in high-Cr heat-resistant steel containing V is influenced mainly by the tempering temperature. A large amount of M_2C was observed in specimens tempered at temperatures below 993 K, whereas MC precipitated instead of M_2C in specimens tempered at temperatures above 1023 K. Onizawa *et al.* [25] found that the growth rate of $Cr_2(C,N)$ in V-containing steels is slower than that in V-free steel. Because of the presence of carbide-forming elements such as Cr, Mo, W, and V, the carbide precipitation behavior in the high-alloy steels becomes complex during tempering. In particular, the effect of alloying elements on the type, distribution, and evolution of carbides related to the secondary hardening phenomenon plays an important role in improving the tempering stability of steels [26–28]. In this paper, we attempt to identify the various nanosized carbide precipitations formed during tempering of Fe–Cr–Mo–W–V hot forging die steels by TEM; we also attempt to determine the specific carbide phase that significantly affects the transformation kinetics characteristics, which can increase the softening resistance greatly.

2. Experimental

2.1. Materials

The studied materials were three commercial hot forging die steels: DM, H21, and H13; Table 1 shows the compositions of the experimental steels. The H21 and H13 steels are conventional hot-work tool steels with excellent service performance. The DM steel is a newly developed steel with a leaner balance of carbide alloying elements for improved high-temperature properties.

Table 1. Normal chemical composition of DM, H21, and H13 steels wt%

Steel	C	Mn	Si	Cr	Mo	W	V	Fe
DM	0.40	0.8	0.3	2.3	1.7	1.7	1.0	Bal.
H21	0.32	0.3	0.3	2.9	—	8.5	0.4	Bal.
H13	0.39	0.4	1.0	5.2	1.4	—	1.0	Bal.

2.2. Tempering stability test

The dimensions of the specimens used for the tempering stability tests were 10 mm × 10 mm × 20 mm. The initial heat-treatment process is described in the following paragraphs. First, the DM, H21, and H13 steel specimens were austenitized for 45 min at 1050, 1080, and 1030°C, respectively, and quenched in oil to room temperature. The quenched specimens of DM, H21, and H13 steels were subsequently tempered twice for 2 h at 625, 620, and 600°C, respectively. A similar hardness of HRC 47 was reached in all of the specimens. Finally, the specimens were additionally tempered for different times at 650°C.

The microstructures of the DM, H13, and H21 steel specimens were examined by scanning electron microscopy (SEM; ZEISS Supra40, Germany) and by TEM (JEOL 2010F, Japan, operated at 200 kV) in conjunction with energy-dispersive spectroscopy (EDS). The specimens for TEM observation were prepared by being thinned by dual-jet electropolishing in a Tenupol dual-jet electropolisher, using an electrolyte consisting of 10vol% perchloric acid with methanol. The electrolyte temperature was maintained at approximately −40°C, and a voltage of 10 V was used for thinning.

2.3. Dilatometry

For the dilatometry investigations, a Bahr DIL-805/D dilatometer was used. Cylindrical specimens of the DM, H21, and H13 steels with a diameter of 4 mm and a length of 10 mm were used. After prior quenching from 1060°C (austenitization time 20 min), the specimens were heated to 750°C at various rates of 0.014, 0.02, 0.03, and 0.05°C/s. The digitally recorded heating dilatograms enabled the continuous heating precipitation (CHP) curves of the experimental steels to be constructed in the system temperature–time according to characteristic points read from the differential curves. Moreover, the microstructures of the specimens were analyzed by SEM (ZEISS Supra40, Germany) after the dilatometry experiments.

3. Results

3.1. Hardness evolution

Fig. 1 shows the hardness curves of the DM, H21, and

H13 steels as functions of the tempering duration at 650°C. The hardness values of all three steels decrease with increasing tempering time, and the slopes of the hardness curves gradually become stable. According to Fig. 1, the initial hardness values of the quenched and tempered DM, H21, and H13 steels are HRC 47.2, 46.7, and 46.5, respectively, and the hardnesses of the three tested steels decrease to HRC 32.6, 30.4, and 25.6, respectively, after the specimens were tempered for 24 h at 650°C. To evaluate the tempering stability of the three steels, we used the tempering kinetic law known as the J–M–A-type equation [29–33], which is represented as

$$\tau = 1 - \exp(-Dt^n) \tag{1}$$

where D is the rate constant for a reaction (at a given temperature) that follows the Arrhenius equation, t is the tempering time, n is the Avrami exponent, which depends on the material and its thermal history, and τ is the tempering ratio, as obtained from Eq. (2):

$$\tau = \frac{H - H_0}{H_\infty - H_0} \tag{2}$$

where H_0, H_∞, and H are the hardness values of the quenched, annealed, and the intermediate states (between the as-quenched and the annealed states), respectively.

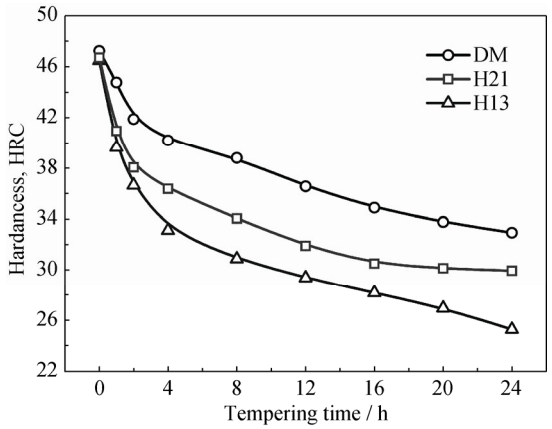

Fig. 1. Hardness as a function of tempering time at 650°C for DM, H21, and H13 steels.

Eq. (1) is represented as a plot of lnln[1/(1−τ)] versus ln$t$, as shown in Eq. (3):

$$\ln\ln\frac{1}{1-\tau} = n\ln t + \ln D \tag{3}$$

The results obtained by plotting Eq. (3) using the values obtained by introducing the measured hardness values (Fig. 1) in Eq. (2) are shown in Fig. 2. The values of the Avrami exponent n of the DM, H21, and H13 steels at 650°C are 0.281, 0.298, and 0.337, respectively. According to the Lifshitz–Slyozov–Wagner theory, when the value of n is approximately 1/3, the coarsening kinetics is controlled by volume diffusion [34–35]. Lindsley *et al.* [36] and Nam *et al.* [37] have reported n values in the range from 0.20 to 0.23 and concluded that the coarsening of carbides is predominantly controlled by the diffusion of carbon along the dislocations and the grain boundaries. The diffusion of the solute atoms during tempering at 650°C in DM and H21 steels is clearly controlled by grain-boundary and volume diffusion, whereas diffusion in H13 steel is controlled by the volume diffusion. In addition, the results indicate that the average rate of precipitation and coarsening of carbides, which plays a key role in determining the tempering stability, is the smallest in the DM steel.

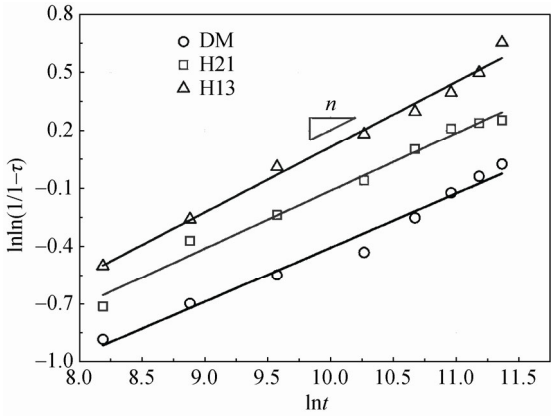

Fig. 2. Avrami exponent n of DM, H21, and H13 steels during tempering at 650°C, where t is the tempering time and τ is the tempering ratio.

3.2. TEM investigations

To study the microstructural evolution of steels during tempering, especially the type, shape, and distribution of carbides, three experimental steels—DM, H21, and H13—were observed by TEM and their fine structures after tempering for 1 and 24 h at 650°C were characterized. Fig. 3 shows the microstructural characteristics of the DM steel after tempering for 1 h. Fig. 3(a) demonstrates a large number of complex entangled dislocations at the martensitic slab boundaries, whereas the grid-like dislocations are found to remain inside the slab. Fig. 3(b) shows the precipitated nanocarbide particles dispersed between the grid-like dislocations. Liu *et al.* [38] found that the dislocations easily entangle around the carbides and form areas with a high concentration of dislocations. He *et al.* [39] revealed that the carbides have a pinning and dragging effect on the dislocations. Therefore, these small granular carbides can greatly hinder the movement of dislocations, thereby affecting the softening process during tempering. Fig. 3(c) shows the strip-like

carbides that precipitate and grow between the martensitic slabs; these carbides are approximately 15–30 nm in thickness and 100 nm in length and are identified as orthorhombic M_3C carbides on the basis of their diffraction spot patterns; detailed information about them is listed in Table 2. Because the alloying elements Mn, Cr, Mo, and W can substantially diffuse into the ferrite during the process of high-temperature tempering at 650°C, they can easily displace the Fe atoms in the cementite to form alloy cementite, as verified by the EDS spectra of carbides (Fig. 3(d)).

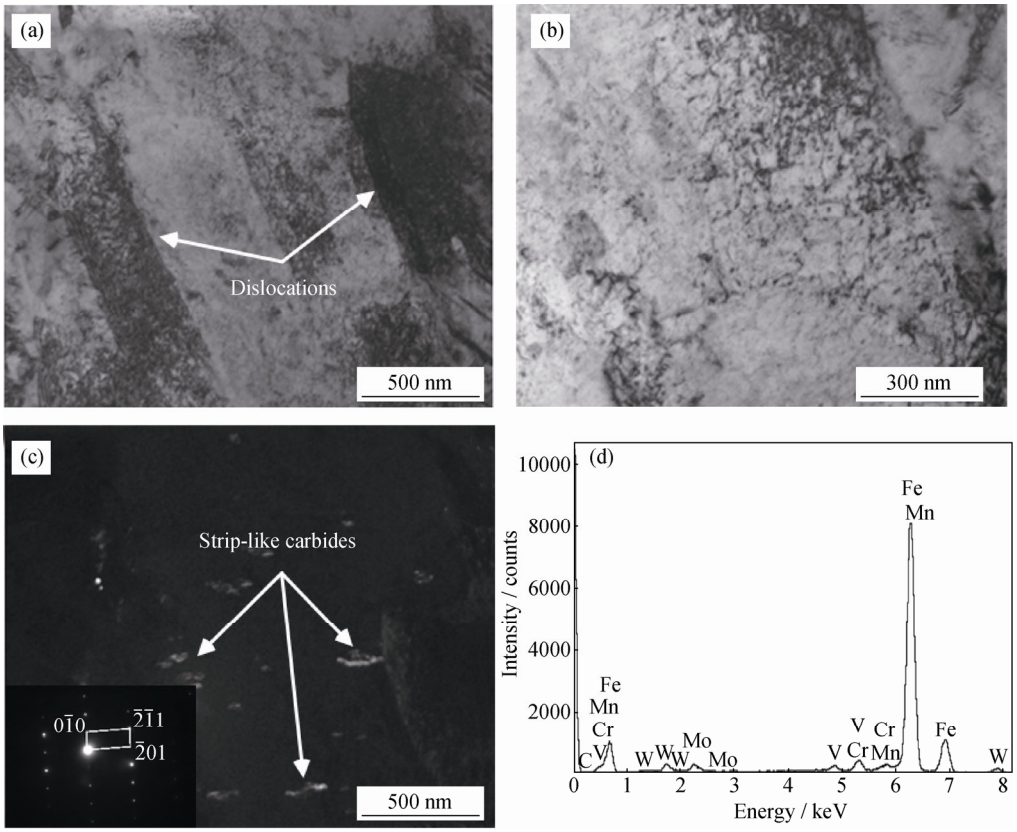

Fig. 3. TEM morphologies of DM steel tempered at 650°C for 1 h: (a) and (b) bright-field images, (c) dark-field image of the strip-like carbides and the corresponding selected-area diffraction (SAD) pattern, and (d) the EDS spectrum of the carbides.

Table 2. Morphologies, sizes, compositions, and types of fine secondary carbides in steel specimens tempered at 650°C for 1 h

Steel	Morphology	Size (length) / nm	Alloying element	Type
DM	Strip	100	Mn, Cr, Mo, W	M_3C
H21	Rod	70	W, V, Cr	M_2C
H13	Rod, Sphere	10–20, 20–30	—	M_2C, M_7C_3

Figs. 4(a) and 4(b) show the TEM images of H21 steel after tempering for 1 h. Fig. 4(a) displays the cellular substructures caused by the aggregation and entanglement of dislocations. Clearly, the dislocations change from cellular dislocations to linear dislocations in some areas. Subsequently, these dislocations arrange themselves to form the slab boundaries, as indicated by the arrow in Fig. 4(a). The circled area in Fig. 4(a) clearly shows the interrupted slab boundaries. Wu *et al.* [40] noted that such a slab boundary results from a series of processes where the parallel dislocation wall is annihilated during migration after heat-induced activation; the disappearance of the interslab boundary induces the merging of adjacent slabs and the subsequent formation of a recrystallized crystal nucleus, eventually leading to the development of a polygonal ferrite structure because of recrystallization. The TEM dark-field image (Fig. 4(b)) shows rod-like carbides with an average size of approximately 70 nm, where the particles are approximately parallel to each other in the slab. These carbides are enriched with W, V, and Cr, as shown in the EDS spectrum in Fig. 4(c). Furthermore, as denoted by the arrows in Fig. 4(b), the dark-field image and the selected-area diffraction (SAD) spot analysis reveal a hexagonal structure for the precipitated phase. According to Ref. [41], the presence of this crystalline structure indicates the formation of M_2C-type carbides in the Fe–Cr–Mo–W–V steel tempered at 650°C.

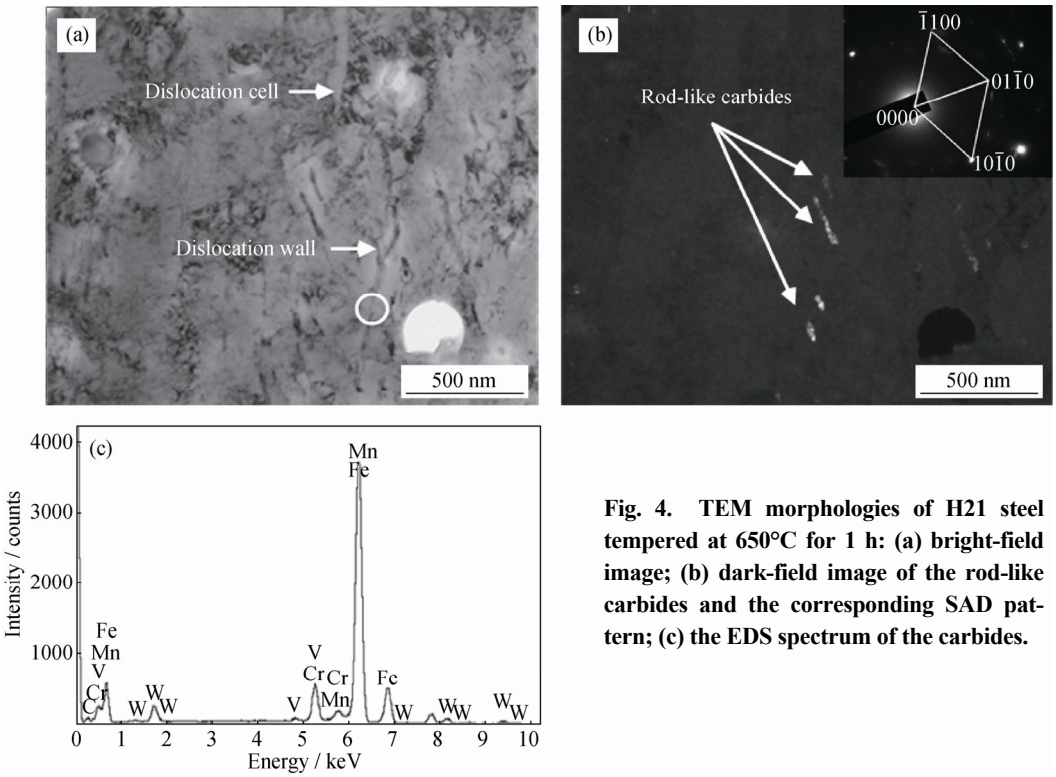

Fig. 4. TEM morphologies of H21 steel tempered at 650°C for 1 h: (a) bright-field image; (b) dark-field image of the rod-like carbides and the corresponding SAD pattern; (c) the EDS spectrum of the carbides.

Fig. 5(a) is the TEM bright-field image of H13 steel after tempering for 1 h. Despite the partial merging of slabs in the steel, the subgrain boundaries at the unrecovered regions remain clearly visible. Meanwhile, the precipitated particles with both coherent and non-coherent contrast are dispersed in the martensitic slabs. The coherently precipitated particles have a diameter of approximately 2 nm and a length of approximately 10–20 nm (Table 2). They are small rod-like particles arranged parallel to each other inside the slabs. As previously discussed, the fine rod-like carbides in a parallel arrangement, denoted by the arrows in Fig. 5(b), are likely M_2C-type carbides. The non-coherent precipitate phase has a size of approximately 20–30 nm, with a spherical shape (Table 2); it nucleates along the grain boundaries and the subgrain boundaries. This type of carbide is the major contributor to the scattering of incident electrons, thereby masking the effect of the matrix. As a result, these particles appear dark and clear in the bright-field image (Fig. 5(a)). The corresponding dark-field image is circled in Fig. 5(b). The authors of previous studies [12,42] have shown that such types of precipitate phase particles with parallelogram shapes are likely M_7C_3-type carbides. The non-coherent carbides nucleated at the boundaries of the slabs are more susceptible to coarsening than the coherent carbides precipitated inside the slabs. This effect is attributed to grain boundaries and dislocations that can form channels for fast atom diffusion, thus facilitating the nucleation and growth of the carbides. Yang *et al.* [43–44] found that the chemical potential of the fine carbide particles is higher than that of the coarse carbide particles and that, as a result, the initially precipitated fine carbide particles re-dissolve and migrate by diffusion toward the large carbide particles and grain boundaries (i.e., Ostwald ripening occurs). At the same time, a significant depletion of the alloying elements and carbon elements inside the grains severely affects the properties of the material. We deduced that, along with the transition from coherent carbides to non-coherent carbides, H13 steel shows a substantial softening phenomenon that agrees well with the change in the H13 steel hardness, which decreases by approximately HRC 7 after 1 h of tempering (Fig. 1(c)).

The TEM image in Fig. 6(a) shows the morphology of DM steel after 24 h of tempering. The bright-field image shows the presence of needle-like carbides and entangled dislocations in the martensitic slabs. The continuous precipitation of granular carbides is generally accepted to effectively prevent the slip of dislocations. As evident in the dark-field image in Fig. 6(b), the intermittent linearly distributed nanosized carbide particles coexist with the needle-like carbide particles; this special morphology is similar to that of the undissolved carbides. Zhou *et al.* [45] argued that such carbides might be formed by the dissolu-

tion and transformation of M_3C alloy cementite. However, the M_3C carbides in the microstructures (Fig. 3(c)) of DM steel have a strip-like shape and a size of approximately 100 nm, whereas the needle-like carbides are more elongated, ranging in length from 130 to 280 nm (Table 3). Previous studies by Bhadeshia *et al.* [46] have suggested that the M_2C carbides first nucleate at the dislocations within the matrix as thin rods along the $<100>_\alpha$ direction, forming a coherent precipitate phase with the matrix and showing a position relationship of $(0001)_{M2C}//(011)_\alpha$ and $[1120]_{M2C}//[100]_\alpha$, which is consistent with the morphology shown in the TEM image in Fig. 6(a). As previously mentioned, during tempering, the non-coherent precipitate phase is coarsened and the coherent precipitated particles gradually dissolve. However, these dissolving carbides are too small to identify by SAD spot analysis. In the case of DM steel, the needle-like M_2C carbides precipitated in the grains are assumed to have experienced a dissolution process after 24 h of tempering (Fig. 6(b)). As a result, the growth of the non-coherent phase promotes recrystallization-induced nucleation, resulting in a substantial decrease in hardness of the DM steels after 24 h of tempering, as shown in Fig. 1(c).

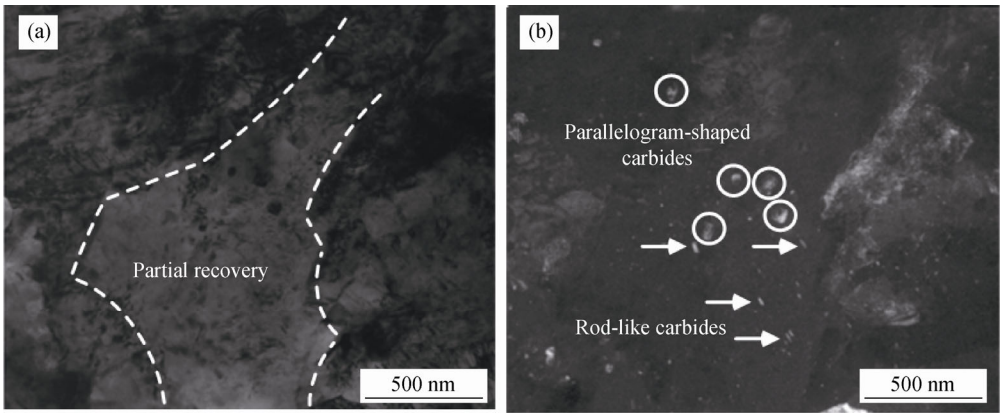

Fig. 5. TEM morphologies of H13 steel after tempering at 650°C for 1 h: (a) bright-field image and (b) dark-field image of the carbides.

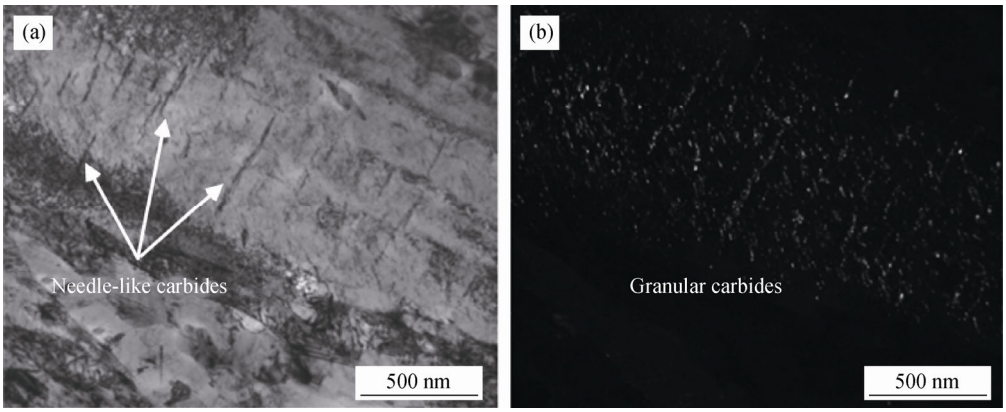

Fig. 6. TEM morphologies of DM steel tempered at 650°C for 24 h: (a) bright-field image and (b) dark-field image of the needle-like carbides.

Table 3. Morphologies, sizes, compositions and types of fine secondary carbides in steel specimens tempered at 650°C for 24 h

Steel	Morphology	Size (length) / nm	Alloying element	Type
DM	Needle	130–280	—	M_2C
H21	Plate	150	W, Cr, Mn, V	M_6C
H13	Sphere	60	—	$M_{23}C_6$

The TEM images in Figs. 7(a) and 7(b) show the morphologies of H21 steel after 24 h of tempering. The bright-field micrograph shows that a large amount of carbides precipitate within the ferrite grains and on dislocations, which mainly exhibit plate-like shapes with an average length of approximately 150 nm, as observed in the dark-field micrograph. These carbides are enriched with W, Cr, Mn, and V, as shown in the EDS spectrum in Fig. 7(c).

Compared with the microstructure of the H21 steel specimen tempered for 1 h (Fig. 4(b)), that of the specimen tempered for 24 h shows agglomeration and coarsening of carbides. Because both M_6C and $M_{23}C_6$ carbides nucleate later than M_2C carbides [47–48] and because they have similar lattice parameters, distinguishing these carbides by SAD spot analysis is difficult. Fortunately, Kurzydłowski *et al.* [49] confirmed that plate-like M_6C precipitates coexist with M_2C precipitates and reported that one of the sides of the plate-like precipitates is always parallel to the axis of the M_2C carbide needle occurring in the same ferrite grain. This observation strongly supports the hypothesis related to these plate-like carbides in the present study. In addition, with prolonged tempering time, M_6C carbides formed by the aforementioned transformation coarsen (by transcrystallization). The result of this transformation is local degradation of H21 steel, and sometimes is total degradation.

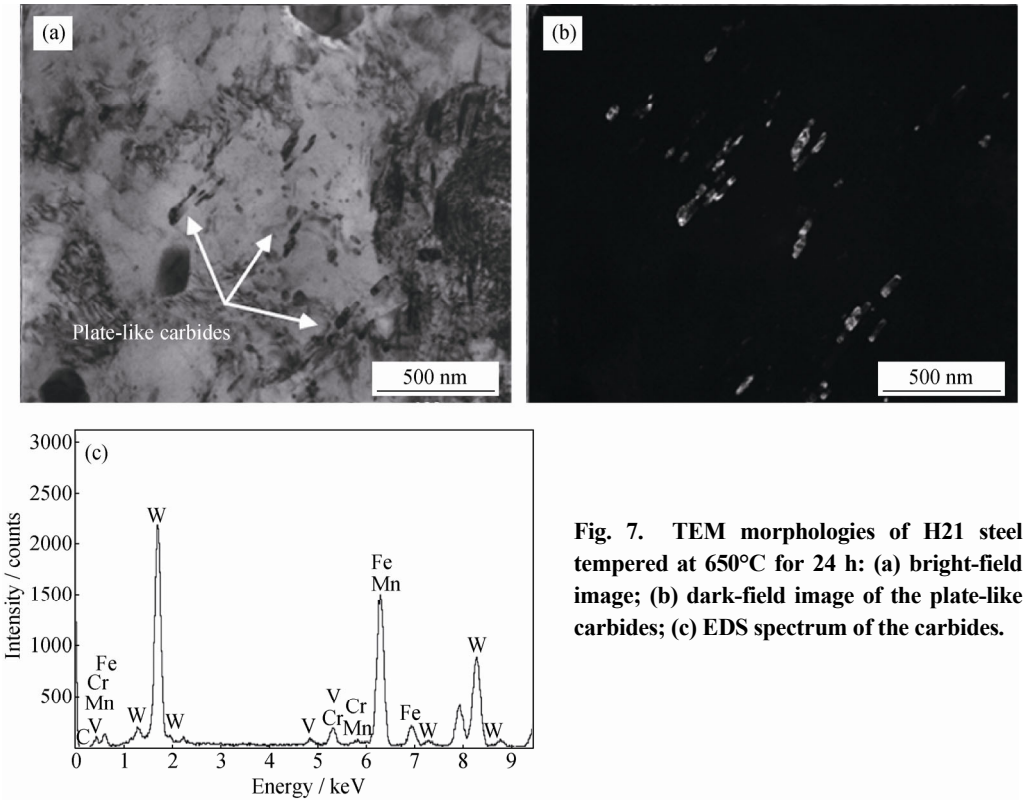

Fig. 7. TEM morphologies of H21 steel tempered at 650°C for 24 h: (a) bright-field image; (b) dark-field image of the plate-like carbides; (c) EDS spectrum of the carbides.

Figs. 8(a) and 8(b) show the TEM bright-field images of different regions of H13 steel after 24 h of tempering. As observed in Fig. 8(a), because a large number of equiaxed band-like carbides participate at the boundaries, the microstructure shows further recovery along with the emergence of polygonal ferrites. Fig. 8(b) displays the microstructural morphology of the intragranular region. Compared to the microstructure of H13 steel after 1 h of tempering (Fig. 5(a)), the width of the intragranular martensitic slabs increases substantially, indicating further merging of the slabs. Meanwhile, irregular-shaped spherical carbides are present in the grains, most likely in the vicinity of the intermittent subgrain boundaries retained after the recovery process. The size of these carbides is approximately 60 nm, and SAD analysis shows that the precipitated carbides belong to the $M_{23}C_6$-type with a face-centered cubic structure (Table 3). Hu *et al.* [50] used the extraction replica method to study the carbide coarsening behavior of H13 steel during the thermal fatigue process. They concluded that $M_{23}C_6$ carbides exhibit two major morphology types: irregular spherical shapes and bar-like shapes. Dudova *et al.* [51], in a study on the process of carbide precipitation during tempering of 10wt% Cr steel, found that, under a high-temperature condition, $M_{23}C_6$ carbides can be divided into two types that exist at high-angle grain boundaries or low-angle slab boundaries. Consequently, the characteristics of the $M_{23}C_6$ carbides observed in the present study agree well with those described in the aforementioned studies. Because the small $M_{23}C_6$ carbides are not thermodynamically stable during tempering, the nanosized $M_{23}C_6$ carbides located at the slab boundaries within the grains tend to dissolve, and the $M_{23}C_6$ carbides on the high-angle grain boundaries undergo coarsening. Because of the slight ef-

fect of the coarsened $M_{23}C_6$ carbides on the pinning of slab boundaries, the slabs quickly merge and disappear with increasing tempering time, ultimately leading to a recrystallization process and the subsequent transformation to form polygonal ferrites. This change plays a substantial role in reducing the hardness of the H13 steel tempered for 24 h (Fig. 1(c)).

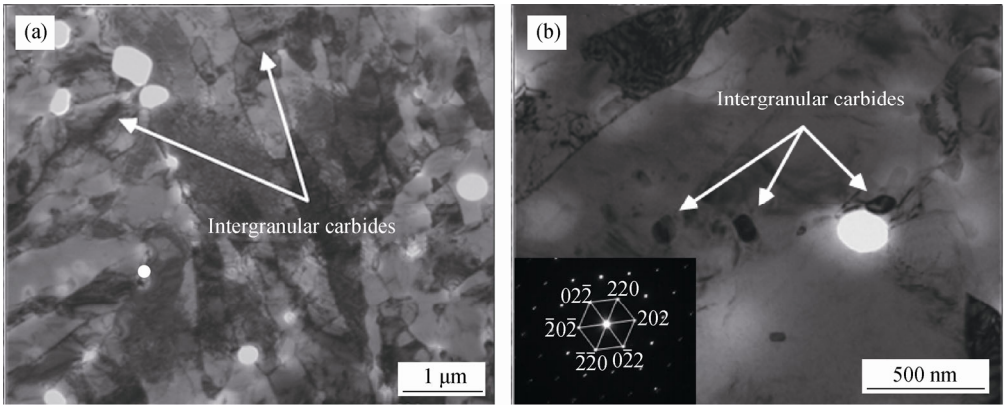

Fig. 8. TEM morphologies of H13 steel after tempered at 650°C for 24 h: (a) bright-field image of the intergranular carbides; (b) bright-field image of the intragranular carbides and the corresponding SAD pattern.

3.3. CHP investigations

Notably, the sequence of the phase transformations strongly affects the tempering stability of the steels. To elucidate the mechanism, we investigated the kinetics of the phase transformations during continuous heating from the as-quenched state of the Fe–Cr–Mo–W–V hot forging die steels using their CHP curves. Fig. 9 shows the variations in the derivatives of dilatometric strain $(\mathrm{d}(\Delta L/L_0)/\mathrm{d}T)$ with temperature, known as CHP curves, for the as-quenched DM, H13, and H21 steels obtained during continuous heating to 750°C at a heating rate of 0.02°C/s.

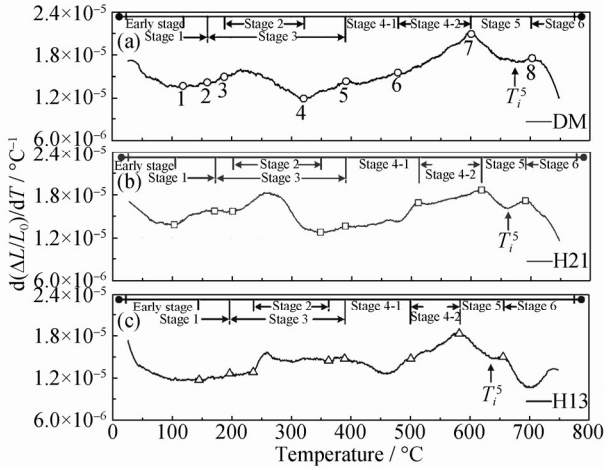

Fig. 9. Variations in the derivatives of the dilatometric strain with respect to the temperature of DM (a), H21 (b), and H13 (c) steels with continuous heating to 750°C at a heating rate of 0.02°C/s.

Fig. 9(a) presents the CHP curve of DM steel, which exhibits eight turning points, dividing the curve into seven stages of phase transformation. The first stage consists of two temperature intervals. The low-temperature interval corresponds to the early stages of decomposition of virgin martensite and ends at 118°C (P1). The high-temperature interval corresponds to the precipitation of carbide ε, which occurs between 118°C (P1) and 159°C (P2). In the early stage, the CHP curve exhibits an abrupt decrease with increasing temperature. A similar phenomenon was reported by Jung *et al.* [52], who combined the electrical resistivity curve and the phase transformation curve of martensite. We speculate that the primary reason for the drastic decrease in the derivative of unit temperature dilatometric strain in this stage is the transformation of the clustering of carbon atoms. After the early stage, i.e., when the temperature is higher than 118°C (P1), the CHP curve fluctuates slightly, corresponding to the formation of transitional ε-carbide. Fig. 10(a) shows the SEM image of DM steel at 118°C (P1); this image reveals the presence of needle-shaped ε-carbides parallel to each other on the martensite lath, marked by a square in the image.

With increasing temperature, the CHP curve enters the third precipitation stage, as shown in Fig. 9(a), which is characterized by a slight decrease in the derivative of unit temperature dilatometric strain. This decrease is mainly caused by the volume contraction due to the transformation of the transitional ε-carbide to cementite in the martensite. The contraction begins at 159°C (P2) and ends at 396°C (P5). Within the range of cementite precipitation, a positive dilatation effect associated with the transition of part of the retained austenite is also observed. This effect is visible within the temperature range from 188 (P3) to 322°C (P4), in agreement with Ref. [53]. Figs. 10(b) and 10(c) show the

SEM images of DM steel at the start and completion of the precipitation of cementite at temperatures of 159 (P2) and 396°C (P5), respectively. The ε-carbides are replaced by rod-like cementites, as shown in the circled portions of Fig. 10(b). By contrast, Fig. 10(c) shows the presence of substantial amounts of rod-like cementites randomly distributed on the lath, as indicated by the square in the figure; it also shows the precipitation of particles at the grain boundary, forming a 50-nm-thick zonal bright region, as indicated by the arrows in the figure.

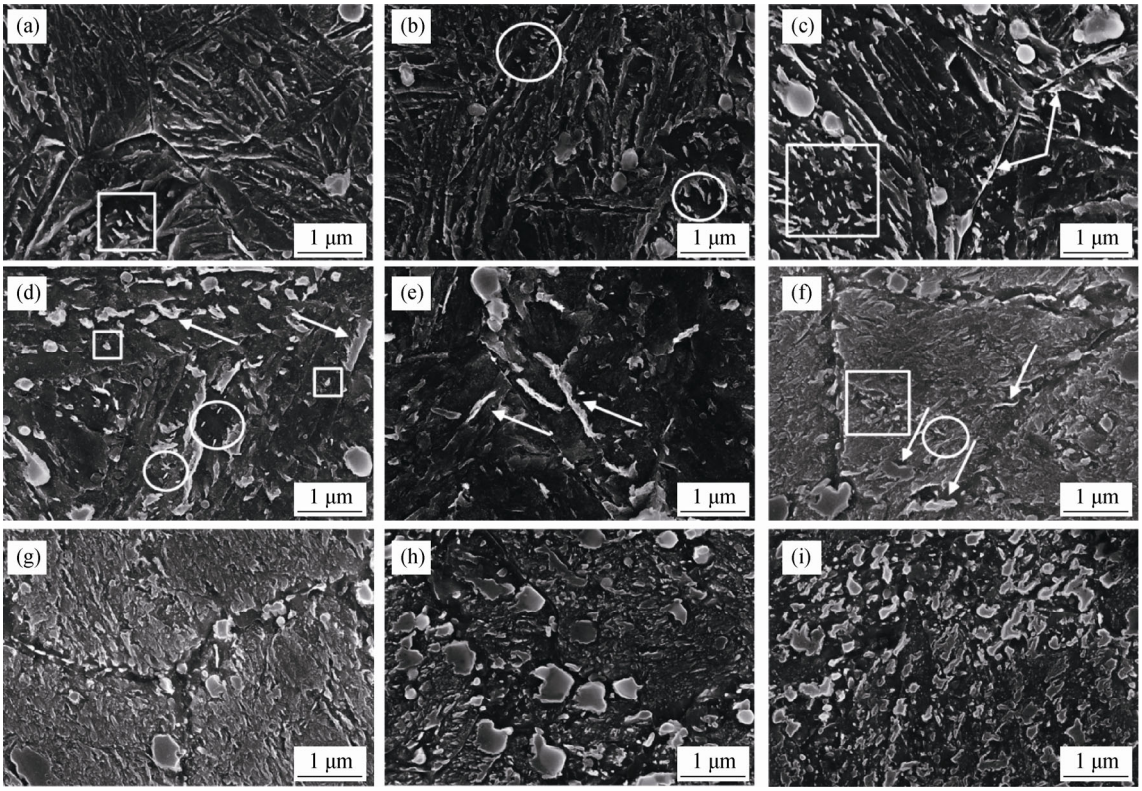

Fig. 10. SEM images showing the precipitates of carbides in DM, H21, and H13 steels, which were continuously heated to a certain temperature at a heating rate of 0.02°C/s, followed by quenching: (a) DM steel at 118°C (P1); (b) DM steel at 159°C (P2); (c) DM steel at 396°C (P5); (d) DM steel at 479°C (P6); (e) DM steel at 602°C (P7); (f) DM steel at 704°C (P8); (g) DM steel at 750°C; (h) H21 steel at 750°C; (i) H13 steel at 750°C.

The fourth precipitation stage of the CHP curve in Fig. 9(a) consists of two temperature intervals according to the change in the derivative of unit temperature dilatometric strain with increasing temperature. The curve exhibits a decrease in low-temperature interval because of the volume expansion. The volume contraction is actually the macroreaction of the lattice contraction caused by the decrease in carbon content, which can be attributed to the *in situ* transformation of M_3C to M_7C_3. However, two overlapped transformations occur with increasing temperature. One is the gradual transformation of alloyed cementites and M_7C_3 carbides to $M_{23}C_6$ carbides; carbon atoms can be dissolved out during this transformation [54]. The other transformation is the growth of intergranular large particles at the expense of smaller intragranular particles. Therefore, carbon atoms would spread from the matrix to the boundary, resulting in lattice expansion [37]. Because of the complex nature of the transformations in the fourth precipitation stage, the critical temperature of the two temperature intervals is difficult to define accurately. In this study, the critical temperature is considered to be 479°C (P6), at which a considerable change in the derivative of unit temperature dilatometric strain is observed. Fig. 10(d) shows the SEM image of DM steel heated to 479°C (P6) and quenched. This image reveals the presence of intragranular and intergranular particles of cementite, M_7C_3, and $M_{23}C_6$ carbides formed in the fourth stage; these particles are marked by circles, squares, and arrows, respectively, in Fig. 10(d). Fig. 10(e) shows an SEM image of the DM steel heated to 602°C (P7) and quenched, where the rod-like carbides are dissolved completely and the carbides at the boundary of the martensite lath grow substantially to approximately 2 μm.

At the fifth precipitation stage of the CHP curve in Fig. 9(a), a significant decrease in $d(\Delta L/L_0)/dT$ occurs, suggest-

ing that large quantities of new carbides precipitate in this stage, which may lead to a decrease in the carbon content of the matrix. The TEM analysis during the aforementioned tempering stability experiments indicated the presence of scattered M_2C carbide precipitates in DM steel tempered at 650°C; these precipitates strongly affect the high-temperature tempering stability of DM steel. These new precipitates are reasonably assumed to correspond to M_2C carbides. The volume contraction related to the precipitation of M_2C carbides occurred at temperatures ranging from 602 (P7) to 704°C (P8). Fig. 10(f) shows an SEM image of DM steel heated to 704°C (P8) and quenched. The strip-shaped carbides distributed near the martensite grain boundary become thicker and transform into globular carbides. In addition, the fine carbides that precipitated along the subgrain boundary, as marked by the square, gradually dissolve, as evident in the circled portion of the subgrain boundary in Fig. 10(f). As previously mentioned, the recovery of the tempered lath martensite microstructures is accompanied by the dissolution of M_2C carbides; thus, 704°C (P8) is confirmed to be the end temperature of the transformation of M_2C carbides.

As shown in Fig. 9(a), the CHP curve exhibits an apparent contraction in the temperature range beyond 704°C (P8), which indicates a faster decrease in carbon content in the last precipitation stage. This effect is attributed to the formation of MC carbides. The transformation of $M_2C \rightarrow M_6C$ and the coarsening of the carbides (e.g., M_6C, M_7C_3, and $M_{23}C_6$) are also possible explanations for the observed contraction. Figs. 10(g), 10(h), and 10(i) show the SEM images of the DM, H13, and H21 steel specimens heated at 750°C. The degree of recovery is the lowest in the case of the DM steel.

Given the temperatures used in the study of tempering stability, the characteristics of the three steels in the fifth precipitation stage are worthy of discussion. A comparison of Fig. 9(a) with Figs. 9(b) and 9(c) reveals that the start temperatures for the transformations of DM, H21, and H13 steels at the fifth precipitation stage are 601, 619, and 582°C, respectively, whereas the end temperatures are 704, 693, and 656°C, respectively. Thus, the end temperature of the transformation of M_2C carbide is the highest in DM steel, and the temperatures of the precipitation of M_2C carbides in the fifth stage in the three steels are approximately 103, 74, and 74°C, respectively. Furthermore, the values of the derivatives of the dilatometric strain in the fifth precipitation stage are approximately 4.4×10^{-6}, 3.0×10^{-6}, and 3.8×10^{-6} °C^{-1}, respectively, for DM, H21, and H13 steels, suggesting that the volume contraction caused by M_2C is the most drastic in the case of the DM steel. That is, the quantity of M_2C carbide precipitations is qualitatively confirmed to be the largest in the case of the DM steel. Compared with the H13 and H21 steels, the DM steel exhibits a higher end temperature for the transformation of M_2C carbide, a wider temperature range of precipitation, and a greater amount of precipitation, indicating its higher tempering stability, as previously discussed.

4. Discussion

Because M_2C carbides are the most important secondary-phase particles with respect to maintaining the tempering stability of DM, H21, and H13 steels at 650°C, the Kissinger thermal analysis method [55] was used to calculate the activation energy values for the precipitation of M_2C carbides in the three experimental steels:

$$\ln\frac{\varphi}{T_i^2} = -\frac{Q}{RT_i} + \text{constant} \tag{4}$$

where φ is the heating rate, which was set as 0.014, 0.02, 0.03, or 0.05°C/s for the calculation; T_i is the temperature corresponding to an inflection point on the curve of the strain-derivative ($\mathrm{d}(\Delta L/L_0)/\mathrm{d}T$); Q is the activation energy for precipitation of M_2C carbides; and R is the gas constant, respectively. The activation energies for the precipitation of M_2C carbides in the DM, H21, and H13 steels are 236.4, 212.0, and 228.9 kJ/mol, respectively (Fig. 11). Borisov *et al.* [56] found that the activation energy of volume diffusion of Mo atoms was 314 kJ/mol in the case of 0.7wt% Mo added to pure iron. In the Mo_2C carbide coarsening experiment conducted by Davies *et al.* [57], the activation energy for the transformation was 290 kJ/mol. Lee *et al.* [56,58] calculated the coarsening kinetics of M_2C carbides in the Fe–14Co–10Ni–0.25C–4Mo alloy system and reported that the activation energy for volume diffusion of Mo atoms was 331–354 kJ/mol. In summary, the activation energy for volume diffusion of Mo atoms and carbide coarsening controlled by the volume diffusion ranges from 290 to 354 kJ/mol in previous studies. In the present study, the activation energy of M_2C carbides is in the range of 212.0–236.4 kJ/mol for the three types of steels, which is slightly lower than the volume diffusion activation energy of Mo atoms. Zhao [59] noted that coherent nucleation of M_2C-type carbides at dislocations is determined by the thermodynamics, crystallographic conditions, and the concentration fluctuations of the alloying elements caused by dislocations. The precipitation of M_2C carbides is controlled by two diffusion processes: the diffusion of alloy elements from the matrix to the dislocation and the diffusion of alloy elements along the

dislocation. The former process is controlled by the volume diffusion of alloy elements. In the latter process, because of a high dislocation density, alloy atoms only need to migrate a small distance to enable the nucleation of M_2C carbides. On the basis of this theory, we concluded that the activation energy for the precipitation of M_2C carbides is intermediate between the activation energy for diffusion along the dislocation channels and that for volume diffusion of alloy elements.

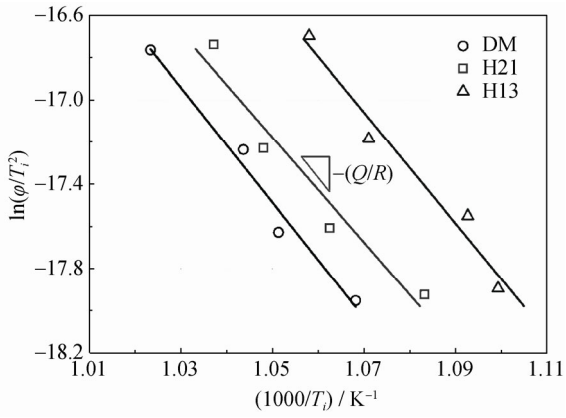

Fig. 11. Kissinger plots of the precipitations of M_2C carbides in DM, H21, and H13 steels, where φ is the constant heating rate, T_i is the temperature corresponding to an inflection point on the curve of the strain-derivative, Q is the activation energy for precipitation, and R is the gas constant.

Notably, among the investigated steels, the DM steel exhibits the highest activation energy (236.4 kJ/mol) for the precipitation of M_2C carbides, although the H13 steel exhibits a similar activation energy. The H21 steel exhibits the lowest activation energy (212.0 kJ/mol). Previous research indicates that the addition of V can reduce the diffusivity of C, Cr, Mo, and Mn atoms via the formation of strong carbides in steel [23–25]. Therefore, the activation energy for the precipitation of M_2C carbides is larger in the DM and H13 steels because of their higher V contents (Table 1). Interestingly, Wen *et al.* [60] utilized three-dimensional atom probe to investigate the effect of V on the microstructure of high-strength steels. They found that, if the V content in the steel is sufficient, V atoms will force almost all C atoms to diffuse toward themselves because of their powerful combining capacity with C atoms, eventually leading to the formation of V-enriched MC carbides. If the V content is low, the amount of V atoms is insufficient to form stable V-enriched MC-type carbides within a limited time; in this case, the nearby Cr and Mo atoms diffuse into carbides, leading to the formation of M_2C and M_6C.

Different transformation mechanisms have been proposed to explain the tempering softening behavior of steels: (i) dissolution of precipitates after being cut by dislocations to a size smaller than the critical size for particle nucleation [61]; (ii) over-aging of precipitates [62]; and (iii) rearrangement of the dislocation substructure into a dislocation subgrain structure with lower internal stress [62–63]. The representative TEM images of the three steels shown in this paper demonstrate that the dimensions and type of carbides change during tempering. As tempering progresses, the matrix defect structure recovers and the rod-like M_2C carbides gradually dissolve in DM and H13 steels, whereas the rod-like M_2C carbides transform to plate-like M_6C carbides in H21 steel. DM and H13 steels seemingly follow the processes (i) and (iii), resulting in the formation of highly stable V-rich MC in sequence. The H21 steel likely follows processes (ii) and (iii). The results presented in this work imply that the calculated activation energy values not only reflect the resistance that impedes carbide precipitation and coarsening but also reflect the resistance to the transformation mechanism of M_2C carbides, which is influenced by the chemical composition, especially the amount of V. Consequently, DM steel exhibits the highest tempering stability among the three investigated Fe–Cr–Mo–W–V hot forging die steels, which is reflected by the DM steel exhibiting the highest Avrami exponent n and the highest activation energy for the precipitation of M_2C carbides during tempering.

5. Conclusions

(1) With increasing tempering time at 650°C, Fe–Cr–Mo–W–V steels exhibited decreased hardness. The microstructures of these steels tempered at 650°C for 1 h consisted mainly of lath martensite, rod-like carbides (M_2C), and parallelogram-shaped intragranular carbides (M_7C_3). With increasing tempering time, rod-like carbide dissolution, plate-like carbide (M_6C) precipitation, and intergranular carbide ($M_{23}C_6$) coarsening became significant.

(2) The CHP curves confirmed the quantity of M_2C carbide precipitated during tempering was the largest in the case of DM steel; M_2C is the most important secondary-phase particle for maintaining the tempering stability of Fe–Cr–Mo–W–V steels.

(3) The activation energy of M_2C carbide precipitation reflects the diffusion of the solute atoms during the precipitation reaction, which is carried out by the volume and dislocation pipe diffusion. DM steel, which exhibited excellent tempering stability, showed the highest activation energy of approximately 236.4 kJ/mol.

Acknowledgement

This work was financially supported by the National Key Technologies R & D Program of China (Nos. 2016YFB0300400 and 2016YFB0300402).

References

[1] D.H. Kim, H.C. Lee, B.M. Kim, and K.H. Kim, Estimation of die service life against plastic deformation and wear during hot forging processes, *J. Mater. Process. Technol.*, 166(2005), No. 3, p. 372.

[2] K. Frisk, Simulation of precipitation of secondary carbides in hot work tool steels, *Mater. Sci. Technol.*, 28(2012), No. 3, p. 288.

[3] S. Nagakura, Y. Hirotsu, M. Kusunoki, T. Suzuki, and Y. Nakamura, Crystallographic study of the tempering of martensitic carbon steel by electron microscopy and diffraction, *Metall. Trans. A*, 14(1983), No. 6, p. 1025.

[4] K.A. Taylor, L. Chang, G.B. Olson, G.D.W. Smith, M. Cohen, and J.B. Vander Sande, Spinodal decomposition during aging of Fe–Ni–C martensites, *Metall. Trans. A*, 20(1989), No. 12, p. 2717.

[5] V.H. Baltazar Hernandez, S.S. Nayak, and Y. Zhou, Tempering of martensite in dual-phase steels and its effects on softening behavior, *Metall. Mater. Trans. A*, 42(2011), No. 10, p. 3115.

[6] L.Q. Xu, D.T. Zhang, Y.C. Liu, B.Q. Ning, Z.X. Qiao, Z.S. Yan, and H.J. Li, Precipitation behavior and martensite lath coarsening during tempering of T/P92 ferritic heat-resistant steel, *Int. J. Miner. Metall. Mater.*, 21(2014), No. 5, p. 438.

[7] G. Ghosh and G.B. Olson, Precipitation of paraequilibrium cementite: Experiments, and thermodynamic and kinetic modeling, *Acta Mater.*, 50(2002), No. 8, p. 2099.

[8] S. Björklund, L.F. Donaghey, and M. Hillert, The effect of alloying elements on the rate of Ostwald ripening of cementite in steel, *Acta Metall.*, 20(1972), No. 7, p. 867.

[9] B. Kim, C. Celada, D. San Martín, T. Sourmail, and P.E.J. Rivera-Díaz-del-Castillo, The effect of silicon on the nano-precipitation of cementite, *Acta Mater.*, 61(2013), No. 18, p. 6983.

[10] G. Miyamoto, J.C. Oh, K. Hono, T. Furuhara, and T Maki, Effect of partitioning of Mn and Si on the growth kinetics of cementite in tempered Fe–0.6 mass% C martensite, *Acta Mater.*, 55(2007), No. 15, p. 5027.

[11] R.C. Thomson and M.K. Miller, The partitioning of substitutional solute elements during the tempering of martensite in Cr and Mo containing steels, *Appl. Surf. Sci.*, 87-88(1995), No. 3, p. 185.

[12] J. Pilling and N. Ridley, Tempering of 2.25 pct Cr–1 pct Mo low carbon steels, *Metall. Trans. A*, 13(1982), No. 4, p. 557.

[13] R.G. Baker and J. Nutting, The tempering of 2.25Cr–1Mo steel after quenching and normalizing, *J. Iron Steel Inst.*, 192(1959), p. 257

[14] A. Inoue and T. Masumoto, Carbide reactions ($M_3C \rightarrow M_7C_3 \rightarrow M_{23}C_6 \rightarrow M_6C$) during tempering of rapidly solidified high carbon Cr–W and Cr–Mo steels, *Metall. Trans. A*, 11(1980), No. 5, p. 739.

[15] P. Chakraborty, V. Kain, P.K. Pradhan, R.K. Fotedar, and N. Krishnamurthy, Corrosion of modified 9Cr–1Mo steel and Indian RAFMS in static Pb–17Li at 773 K, *J. Fusion Energy*, 34(2015), No. 2, p. 293.

[16] R. Viswanathan and W.T. Bakker, Materials for ultrasupercritical coal power plants—Boiler materials: Part 1, *J. Mater. Eng. Perform.*, 10(2001), No. 1, p. 81.

[17] S.I. Porollo, A.M. Dvoriashin, Y.V. Konobeev, and F.A. Gamer, Microstructure and mechanical properties of ferritic/martensitic steel EP-823 after neutron irradiation to high doses in BOR-60, *J. Nucl. Mater.*, 329-333(2004), p. 314.

[18] R.L. Klueh, Elevated temperature ferritic and martensitic steels and their application to future nuclear reactors, *Int. Mater. Rev.*, 50(2005), No. 5, p. 287.

[19] S. Moniri, M. Ghoranneviss, M.R. Hantehzadeh, and A. Salar Elah, Nano-scale precipitates of reduced activation steels for the application of nuclear fusion reactors, *J. Fusion Energy*, 34(2015), No. 3, p. 449.

[20] M. Nurbanasari, P. Tsakiropoulos, and E.J. Palmiere, Microstructural evolution of a heat-treated H23 tool steel, *Int. J. Miner. Metall. Mater.*, 22(2015), No. 3, p. 272.

[21] T. Mukherjee, *Materials for Metal Cutting*, ISI Publication, London, 1970, p. 80.

[22] Y.T. Zhang, L.D. Miao, X.J. Wang, H.Q. Zhang, and J.F. Li, Evolution behavior of carbides in 2.25Cr–1Mo–0.25V steel, *Mater. Trans.*, 50(2009), No. 11, p. 2507.

[23] Y. Zhang, *Application of Phase Equilibrium Thermodynamic Method in Alloy Design for High Carbon Alloy Steel with Ultra-Fine Carbides* [Dissertation], Dalian Maritime University, Dalian, 2007.

[24] R. Ishii, Y. Tsuda, M. Yamada, and K. Kimura, Fine precipitates in high chromium heat resisting steels, *Tetsu-to-Hagane*, 88(2002), No. 1, p. 36.

[25] T. Onizawa, T. Wakai, M. Ando, and K. Aoto, Effect of V and Nb on precipitation behavior and mechanical properties of high Cr steel, *Nucl. Eng. Des.*, 238(2008), No. 2, p. 408.

[26] R.A. Mesquita and H.J. Kestenbach, Influence of silicon on secondary hardening of 5wt% Cr steels, *Mater. Sci. Eng. A*, 556(2012), p. 970.

[27] A. Medvedeva, J. Bergström, S. Gunnarsson, and J. Andersson, High-temperature properties and microstructural stability of hot-work tool steels, *Mater. Sci. Eng. A*, 523(2009), No. 1-2, p. 39.

[28] P. Bała and J. Pacyna, The kinetics of phase transformations during tempering in high-speed steels, *J. Ach. Mater. Manuf. Eng.*, 23(2007), No. 2, p. 15.

[29] W.A. Johnson and R.F. Mehl, Reaction kinetics in processes of nucleation and growth, *Trans. AIME*, 135(1939), No. 8, p. 416.

[30] M. Avrami, Kinetics of phase change. I General theory, *J. Chem. Phys.*, 7(1939), No. 12, p. 1103.

[31] M. Avrami, Kinetics of phase change. II Transformation-time relations for random distribution of nuclei, *J. Chem. Phys.*, 8(1940), No. 2, p. 212.

[32] M. Avrami, Granulation, phase change, and microstructure kinetics of phase change. III, *J. Chem. Phys.*, 9(1941), No. 2,

p. 177.

[33] E. López-Martínez, O. Vázquez-Gómez, H.J. Vergara-Hernández, and B. Campillo, Effect of initial microstructure on austenite formation kinetics in high-strength experimental microalloyed steels, *Int. J. Miner., Metall. Mater.*, 22(2015), No. 12, p. 1304.

[34] I.M. Lifshitz and V.V. Slyozov, The kinetics of precipitation from supersaturated solid solutions, *J. Phys. Chem. Solids*, 19(1961), No. 1-2, p. 35.

[35] C. Wagner, Theorie der alterung von niederschlägen durch umlösen, *Z. Elektrochem.*, 65(1961), No. 7-8, p. 581.

[36] B.A. Lindsley and A.R. Marder, Solid particle erosion of an Fe–Fe_3C metal matrix composite, *Metall. Mater. Trans. A*, 29(1998), No. 3, p. 1071.

[37] W.J. Nam and C.M. Bae, Coarsening behavior of cementite particles at a subcritical temperature in a medium carbon steel, *Scripta Mater.*, 41(1999), No. 3, p. 313.

[38] L.R. Liu, T. Jin, N.R. Zhao, X.F. Sun, H.R. Guan, and Z.Q Hu, Formation of carbides and their effects on stress rupture of a Ni-base single crystal superalloy, *Mater. Sci. Eng. A*, 361(2003), No. 1-2, p. 191.

[39] L.Z. He, Q. Zheng, X.F. Sun, H.R. Guan, Z.Q. Hu, A.K. Tieu, C. Lu, and H.T. Zhu, Effect of carbides on the creep properties of a Ni-base superalloy M963, *Mater. Sci. Eng. A*, 397(2005), No. 1, p. 297.

[40] H.B. Wu, S.W. Yan, S.Q. Yuan, C.J. Shang, X.M. Wang, and X.L. He, Effect of isothermal relaxation on thermo-stability of non-equilibrium microstructure in micro-alloyed steel, *Acta Metall. Sinica*, 41(2005), No. 4, p. 385.

[41] M.T.C. Ferrari, J. Andersson, and M. Kvarnström, Influence of lowered austenitisation temperature during hardening on tempering resistance of modified H13 tool steel (Uddeholm Dievar), *Int. Heat Treat. Surf. Eng.*, 7(2013), No. 3, p. 129.

[42] N. Gope, A. Chatterjee, T. Mukherjee, and D.S. Sarma, Influence of long-term aging and superimposed creep stress on the microstructure of 2.25Cr–1Mo steel, *Metall. Trans. A*, 24(1993), No. 2, p. 315.

[43] R.C. Yang, K. Chen, H.X. Feng, and H. Wang, Determination and application of larson-miller parameter for heat resistant steel 12CrlMoV and 15CrMo, *Acta Metall. Sinica (Engl. Lett.)*, 17(2004), No. 4, p. 471.

[44] R.C. Yang, K. Chen, H.X. Feng, and H. Wang, Variation of substructures of pearlitic heat resistant steel after high temperature aging, *Acta Metall. Sinica (Engl. Lett.)*, 17(2004), No. 4, p. 477.

[45] Q.C. Zhou, X.C. Wu, N.N. Shi, J.W. Li, and N. Min, Microstructure evolution and kinetic analysis of DM hot-work die steels during tempering, *Mater. Sci. Eng. A*, 528(2011), No. 18, p. 5696.

[46] H.K.D.H. Bhadeshia and R.W.K. Honeycombe, *Steels Microstructure and Properties*, 3rd Ed., Elsevier, Oxford, 2006, p. 195.

[47] S. Karagöz, H.F. Fischmeister, H.O. Andrén, and G.J. Cai, Microstructural changes during overtempering of high-speed steels, *Metall. Trans. A*, 23(1992), No. 6, p. 1631.

[48] J. Guo, H.W. Qu, L.G. Liu, Y.L. Sun, Y. Zhang, and Q.X. Yang, Study on stable and meta-stable carbides in a high speed steel for rollers during tempering processes, *Int. J. Miner. Metall. Mater.*, 20(2013), No. 2, p. 146.

[49] K.J. Kurzydłowski and W. Zieliński, $Mo_2C \rightarrow M_6C$ carbide transformation in low alloy Cr–Mo ferritic steels, *Met. Sci.*, 18(1984), No. 4, p. 223.

[50] X.B. Hu, L. Li, X.C. Wu, and M. Zhang, Coarsening behavior of $M_{23}C_6$ carbides after ageing or thermal fatigue in AISI H13 steel with niobium, *Int. J. Fatigue*, 28(2006), No. 3, p. 175.

[51] N. Dudova and R. Kaibyshev, On the precipitation sequence in a 10%Cr steel under tempering, *ISIJ Int.*, 51(2011), No. 5, p. 826.

[52] M. Jung, S.J. Lee, and Y.K. Lee, Microstructural and dilatational changes during tempering and tempering kinetics in martensitic medium-carbon steel, *Metall. Mater. Trans. A*, 40(2009), No. 3, p. 551.

[53] P. Bała, The kinetics of phase transformations during tempering of tool steels with different carbon content, *Arch. Metall. Mater.*, 54(2009), No. 2, p. 491.

[54] P. Tao, C. Zhang, Z.G. Yang, and H. Takeda, Evolution of second phase in 2.25Cr–1Mo–0.25V steel weld metal during high temperature tempering, *Acta Metall. Sinica*, 45(2009), No. 1, p. 51.

[55] J.G. Jung, M. Jung, S. Kang, and Y.K. Lee, Precipitation behaviors of carbides and Cu during continuous heating for tempering in Cu-bearing medium C martensitic steel, *J. Mater. Sci.*, 49(2014), No. 5, p. 2204.

[56] H.M. Lee and S.M. Allen, Coarsening resistance of M_2C carbides in secondary hardening steels: Part III. Comparison of theory and experiment, *Metall. Trans. A*, 22(1991), No. 12, p. 2877.

[57] D.M. Davies and B. Ralph, Field ion microscopic study of quenched and tempered Fe–Mo–C, *J. Iron Steel Inst.*, 210(1972), No. 4, p. 262.

[58] H.M. Lee, S.M. Allen, and M. Grujicic, Coarsening resistance of M_2C carbides in secondary hardening steels: Part I. Theoretical model for multicomponent coarsening kinetics, *Metall. Trans. A*, 22(1991), No. 12, p. 2863.

[59] Z.Y. Zhao, Studing status on the secondary hardening phenomenon in ultra-high strength steels, *J. Aeronaut. Mater.*, 22(2002), No. 4, p. 46.

[60] T. Wen, X.F. Hu, Y.Y. Song, D.S. Yan, and L.J. Rong, Carbides and mechanical properties in an Fe–Cr–Ni–Mo high-strength steel with different V contents, *Mater. Sci. Eng. A*, 588(2013), p. 201.

[61] S. Suresh, *Fatigue of Materials*, *Cambridge Solid State Science Series* [Dissertation], Cambridge University, Cambridge, 1991.

[62] A.F. Armas, C. Petersen, R. Schmitt, M. Avalos, and I. Alvarez-Armas, Mechanical and microstructural behaviour of isothermally and thermally fatigued ferritic /martensitic steels, *J. Nucl. Mater.*, 307-311(2002), p. 509.

[63] J. Sjöström, *Chromium Martensitic Hot-work Tool Steels Damage*, *Performance and Microstructure* [Dissertation], Karlstad University, Karlstad, 2004.